Heaviside projection based aggregation in stress constrained topology optimization

Cunfu Wang Xiaoping Qian*

Department of Mechanical Engineering,
University of Wisconsin-Madison,
1513 University Avenue, Madison, WI 53706

Abstract

The paper introduces an approach to stress constrained topology optimization through Heaviside projection based constraint aggregation. The aggregation is calculated by integrating Heaviside projected local stresses over the design domain and then it is normalized over the total material volume. Effectively, the normalized integral measures the volume fraction of the material that has violated the stress constraint. Hence with the Heaviside aggregated constraint, we can remove the stress failed material from the final design by constraining the integral to a threshold value near zero. An adaptive strategy is developed to select the threshold value for ensuring that the optimized design is conservative. By adding a stress penalty factor to the integrand, the Heaviside aggregated constraint can further penalize high stresses, and becomes more stable and less sensitive to the selection of the threshold value. Our 2D and 3D numerical experiments demonstrate that the single Heaviside aggregated stress constraint can efficiently control the local stress level. Compared to the traditional approaches based on the Kreisselmeier-Steihauser and p-norm aggregations, the Heaviside aggregation based single constraint can substantially reduce computational cost on sensitivity analysis. These advantages make it possible to apply the proposed approach to large scale stress-constrained problems.

Keywords Topology optimization, Stress constraints, Constraint aggregation, Heaviside aggregation, Three dimensional (3D)

1 Introduction

Structural topology optimization [1] aims to find the optimal material distribution within a given design domain to improve the prescribed performance of structures. It has been successfully used in product design, especially in conceptual design phase, for a host of problems. Topology optimization under stress constraint remains an interesting and challenging research topic for a couple of reasons.

The first challenge of topology optimization under stress constrains is the singularity issue. The singularity phenomenon was first observed in truss optimization by Sved

*Corresponding author. Email: qian@engr.wisc.edu

and Ginos [2]. They demonstrated that for a three-bar design problem, one of the bars should vanish in the optimum solution. However, when the cross-sectional area of that bar approaches 0, the stress in that bar would violate the stress constraint and prevent the elimination. It was further found that the global optima of the stress constrained problem often exists in lower dimensional subspaces of the feasible design space [3, 4], which are often inaccessible for the gradient-based optimization algorithms. The singularity issue also exists in the density-based topology optimization, in which elements with low densities would have high stresses exceeding the prescribed limit. Hence it is difficult to remove low densities and obtain black-and-white layout. One way to resolve the singularity problem is to relax the stress constraints and make the optima accessible. The relaxation approaches include the ε-relaxation [5] and pq-relaxation [6]. The concept of 'relaxed' stress is also introduced in [7]. The stress for intermediate densities is penalized to achieve black-and-white solutions. It turns out that the 'relaxed' stress can successfully avoid the singularity issue since it allows zero stress state for void material. Recently, a cosine-type relaxation scheme is proposed by [8] to relax stress constraints and it is used in the wrinkle-free design of thin membrane structures.

The second challenge is that the stress constraint is inherently local, usually enforced, e.g. through an element-wise measure. It thus leads to a large number of stress constraints. As such, the number of optimization variables for the density-based topology optimization is of the same order as the number of local stress constraints. Hence, sensitivity analysis becomes extremely time consuming whether with either the direct method or the adjoint method [9]. To resolve this issue, active-set strategies [10] can be applied to consider only potentially dangerous stress constraints. Another resolution is to aggregate the local constraints into a single global constraint, commonly, based on the Kreisselmeier-Steihauser (KS) or the p-norm function [10, 11]. As the single aggregated, global constraint cannot effectively control the local stress level, multiple global constraints are employed in [7, 12, 13] and different grouping strategies are also studied. To futher improve the effectiveness of global constraints, the active-set strategy can also be applied to reduce the number of stresses in each group [14]. Recently, a p-norm correction method is proposed to make the aggregated constraints work efficiently [15]. Evaluation of different aggregation approaches can be found in [16], in which the effect of the number of constraints and the aggregation parameters are also investigated.

It should be noted that although it is straightforward to extend existing aggregation approaches to three-dimensional (3D) problems, 3D designs considering stress constraints rarely appear in the literature. This can in part be ascribed to the fact that, for 3D problems, a large number of the KS or the p-norm aggregated constraints are needed in order to efficiently control the local stress level, which leads to the tremendous computing workload in sensitivity analysis. Therefore, a stress-constrained topology optimization method that can be applicable to 3D problems remains an important research topic.

Existing approaches to aggregate such local constrains, e.g. through KS functions or p-norm, are ineffective when the problem size becomes large in practical setting. The effect of these aggregations is dominated by maximum constraint violations. However, for fully-stressed designs in stress-constrained optimization, many elements would have same constraint values, i.e. near the stress limit. These aggregations would lead to very coarse approximations of the constraints. Therefore, in this paper, we choose to study Heaviside aggregation. Heaviside function involves sharp transition at 0/1 location, i.e. precisely at the stress limit. Larger number of stress constraints do not worsen the constraint aggregation. Therefore, they are more effective in dealing with large number of local

stress constraints.

In this work, we develop a Heaviside projection based aggregation approach for aggregating local stress constraints into one constraint. This is inspired by the recent success of Heaviside aggregation, i.e. Heaviside projection based integral [17], to enforce pointwise overhang angle constraint to obtain support-free optimal designs. Here, the von Mises yield criterion is adopted to evaluate whether the material fails or not. The relaxation strategy introduced in [7] is applied to remedy the singularity problem. Our main concern is on developing a new way to enforce the element-wise local stress constraints. We apply the Heaviside function as an indicator to show the state of the material (safe or failed). If the stress exceeds the yield limit, the indicator function is marked as 1; otherwise 0. Then by integrating the indicator function over the whole design domain and normalizing over the total volume, we obtain the integral of Heaviside projection, which effectively means the volume fraction of the yielded material. As our objective is to make the stress constraint satisfied at every material point, all we need to do is to push the yielded material away, which can be implemented by constraining the Heaviside projection based integral (HPI) to be 0. Based on such Heaviside aggregation, a single global aggregated constraint is constructed. In practice, a smoothed Heaviside function is used as the stress state indicator for differentiability, and a small positive value ϵ rather than 0 is applied to bound the integral. In addition, a stress penalty factor is added into the integrand of the constraint to further penalize high stresses. With the stress factor, the stress constraint has a flavor of the p-norm in low order, and dees not have to force the material to change between two states, safe or failed. Hence, the stress constraint becomes more stable and thus less sensitive to the selection of ϵ. The selection of ϵ is the key to successful enforcement of the stress constraint. If ϵ is too large, the global constraint would not be tight enough to remove the yielded material volume; if ϵ is too small, an over-conservative design would be obtained. In order to get an appropriate threshold ϵ, an adaptive scheme based on the gap between the maximum stress and the prescribed limit is also proposed. As the effectiveness of the global constraint is insensitive to the number of local constraints, it is applicable to large-scale problems.

The remainder of the paper is organized as follows. Section 2 reviews stress constraints in topology optimization and the traditional approaches based on the KS or the p-norm function. In Section 3, our approach to stress-constrained problem through the Heaviside projection based integral is proposed. Section 4 presents the optimization formulation. The sensitivity analysis of the stress constraint is described in Section 5. In Section 6, both the 2D and 3D numerical examples are studied to demonstrate the effectiveness of the proposed approach. Finally, conclusions are drawn in Section 7.

2 Stress constraints in density-based topology optimization

In this section, we introduce the criteria to measure the failure of the material and briefly review the state-of-the-art of the stress constraints in density-based topology optimization.

2.1 Stress measure

The von Mises stress is commonly used to predict the yielding of ductile materials under a complex loading condition. It is chosen as the stress measure in our work. The von Mises stress can be evaluated through tensor manipulations of the deviatoric stress as

$$\sigma^{\mathrm{v}} = (\frac{3}{2}\boldsymbol{\sigma}^{\mathrm{d}} \cdot \boldsymbol{\sigma}^{\mathrm{d}})^{\frac{1}{2}},$$

where $\boldsymbol{\sigma}^{\mathrm{d}}$ can be expressed in terms of the full stress tensor as

$$\boldsymbol{\sigma}^{\mathrm{d}} = \boldsymbol{\sigma} - \frac{1}{3}\mathrm{tr}(\boldsymbol{\sigma})\mathbf{I},$$

where the stress tensor $\boldsymbol{\sigma}$ is defined as

$$\boldsymbol{\sigma}(\mathbf{u}) = 2\mu\nabla\mathbf{u} + \lambda(\nabla \cdot \mathbf{u})\mathbf{I}, \tag{1}$$

where μ and λ are the Lamé constants and $\mathbf{u}$ represents the displacement vector.

For the material with intermediate densities $\bar{\rho}$, the von Mises stress can be penalized to achieve black-and-white layouts [7]. The penalized σ^{v} reads

$$\sigma^{\mathrm{v}} = \eta_s(\bar{\rho})\sigma_0^{\mathrm{v}}, \tag{2}$$

where σ_0^{v} is the von Mises stress of solid material. For the selection of the penalization term $\eta_s(\bar{\rho})$, it should first ensure that σ^{v} yields the proper values for void and solid materials, then make the appearance of intermediate densities unproportionately expensive [12, 13]. In our work, $\eta_s(\bar{\rho})$ is selected as suggested in [7, 12]

$$\eta_s(\bar{\rho}) = \bar{\rho}^{\frac{1}{2}}. \tag{3}$$

It should be noted that this kind of selection of $\eta_s(\bar{\rho})$ aims to obtain black-and-white designs and has no physical meaning as discussed in [10]. But it can successfully avoid the singularity issues in stress-based topology optimization since it allows for zero stress state of void material [7].

2.2 Stress constraints

As the strength of a material is considered in the density-based topology optimization, the stress should satisfy constraint at every point in the design domain. When the finite element method is used to conduct analysis, it requires that stress of each element should be smaller than the prescribed limit $\bar{\sigma}$. That is

$$\sigma_e^{\mathrm{v}} \leq \bar{\sigma}, \quad e = 1, 2, \cdots, N, \tag{4}$$

where the lower case e represents the element index and N is the total number of finite elements. Equation (4) indicates that the number of stress constraints is equal to the number of finite elements. In addition, the number of optimization variables is also comparable to that of elements in the density-based topology optimization. As a result, whether the direct or the adjoint method is utilized for sensitivity analysis, it would be time-consuming to calculate sensitivities of the element-wise stress constraints. This is because we need to conduct N pseudo analyses in the direct method or solve N adjoint

equations in the adjoint method [9]. Further, a large number of stress constraints can also make the optimization problem highly nonlinear and difficult to converge. Therefore, different schemes have been introduced to reduce the number of stress constraints.

A single global constraint is introduced in [10, 11] to replace local stress constraints in (4). The global constraint reads

$$\sigma_{\max}^{\mathrm{v}} = \max_{e=1,\cdots,N}(\sigma_e^{\mathrm{v}}) \leq \bar{\sigma}. \tag{5}$$

In practice, the maximum operation is approximated by the KS or the p-norm function for differentiability. The KS function is defined as

$$\sigma_{\mathrm{KS}} = \frac{1}{\eta} \ln \sum_{i=1}^{N} e^{\eta \sigma_i^{\mathrm{v}}}, \tag{6}$$

where η is the aggregation parameter of the KS function. And the p-norm function reads

$$\sigma_{\mathrm{PN}} = \left[\sum_{i=1}^{N} (\sigma_i^{\mathrm{v}})^P \right]^{\frac{1}{P}}, \tag{7}$$

where P is the p-norm parameter. Both the KS and the p-norm functions can approach the maximum stress $\sigma_{\max}^{\mathrm{v}}$ by using large aggregation parameters η and P. That is

$$\begin{aligned} \lim_{\eta \to \infty} \sigma_{\mathrm{KS}} &= \sigma_{\max}^{\mathrm{v}}, \\ \lim_{P \to \infty} \sigma_{\mathrm{PN}} &= \sigma_{\max}^{\mathrm{v}}. \end{aligned} \tag{8}$$

The large parameters η and P can reduce approximation error, but can simultaneously make the optimization problem difficult to solve with a gradient-based optimization algorithm [16]. Therefore, relative small η and P are preferred in practice. However, using one global stress with the small parameters η and P cannot efficiently control the local stresses due to rough approximation of the maximum stress. As a compromise, the local constraints are divided into multiple groups and aggregated with the KS or the p-norm functions [7, 12, 13]. The grouping strategy and the selection of group number can influence the final design. With more groups applied in the optimization, a more precise approximation of the local constraints can be achieved, however, the computational cost would be increased accordingly. Hence, one has to make a trade off between the computational cost and the approximation accuracy with the KS function based or p-norm based approach.

3 Stress aggregation through Heaviside projection based integral

In this section, we introduce our Heaviside aggregation form for a single, integral form of stress constraint. It is through Heaviside projection based integral (HPI). First, a Heaviside function is introduced as an indicator to show whether the stress constraint is violated. Then, a single constraint is constructed based on the HPI and its physical meaning is explained. Finally, we analyze the computational time saving of the proposed approach compared with the conventional approaches based on the KS and p-norm aggregations.

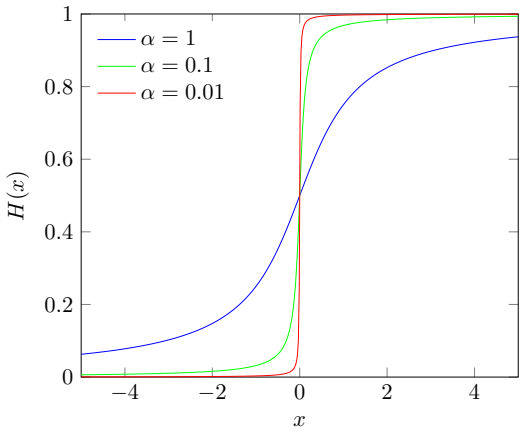

Figure 1: A smooth Heaviside function with different α.

3.1 Stress state indicator

When the von Mises yield criterion is adopted, we need to determine whether the stress exceeds the safe limit of the material. Then the state (safe or failed) of the material can be indicated from the Heaviside function as

$$H(\frac{\sigma^{\mathrm{v}} - \bar{\sigma}}{\bar{\sigma}}) = \begin{cases} 1 & \sigma^{\mathrm{v}} > \bar{\sigma} \\ 0 & \sigma^{\mathrm{v}} \leq \bar{\sigma}, \end{cases} \tag{9}$$

where $\bar{\sigma}$ is the prescribed limit. If the von Mises stress exceeds the limit, the indicator function $H(\frac{\sigma^{\mathrm{v}}-\bar{\sigma}}{\bar{\sigma}})$ returns 1; otherwise returns 0. As the stress state indicator function (9) is utilized to form the stress constraint, we use a smooth Heaviside function for differentiability. It is defined as

$$H_\alpha(x) = 0.5(1 + \frac{2}{\pi}\arctan(\frac{x}{\alpha})), \tag{10}$$

where α is the Heaviside parameter to control the sharpness of $H_\alpha(x)$. The smooth Heaviside function with different α is shown in Fig. 1. It can be observed that the smooth function becomes steeper when α gets smaller and it converges to the exact Heaviside function when α approaches 0.

Figure 2 plots the von Mises stress for the optimized design of the 2D L-bracket problem (see Section 6.1) and the corresponding indicator functions. We select $\bar{\sigma} = 200$ herein for better visualization. For the stress distribution in Fig. 2(a), by using the exact Heaviside function, Figure 2(b) clearly indicates where the material has failed. The stress states based on the smooth Heaviside function of different α are shown in Fig. 2(c) and (d). We can observe that, when using very small α, the smooth Heaviside function can also clearly indicate the stress state as shown in Fig. 2(d). When a relative large α is applied in Fig. 2(c), blur regions appear in the stress state indication. In the case, the indicator faction (10) cannot accurately represent the state of the stresses that are close to the limit.

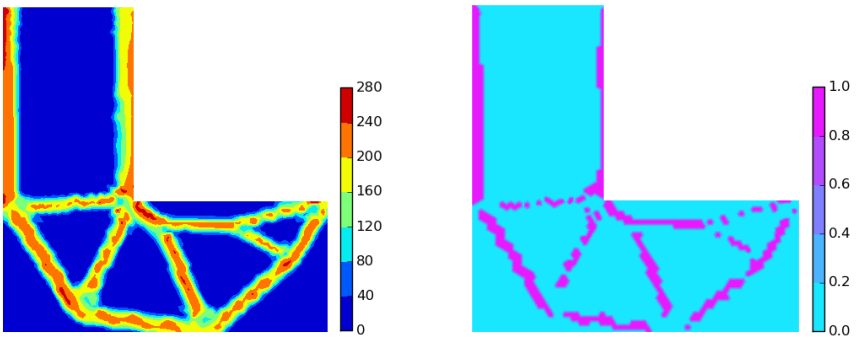

(a) Von mises stress (b) $H(\frac{\sigma^{\mathrm{v}}-\bar{\sigma}}{\bar{\sigma}})$

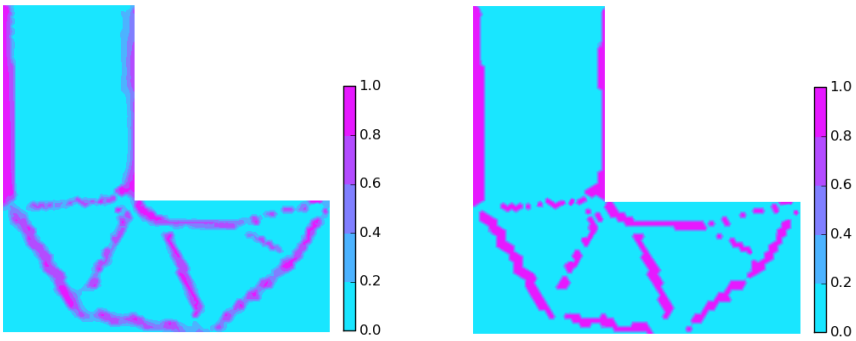

(c) $H_{0.1}(\frac{\sigma^{\mathrm{v}}-\bar{\sigma}}{\bar{\sigma}})$ (d) $H_{0.001}(\frac{\sigma^{\mathrm{v}}-\bar{\sigma}}{\bar{\sigma}})$

Figure 2: Von Mises stress and its Heaviside projections. (a) The von Mises stress distribution, (b) the stress state indication based on the exact Heaviside function, (c)(d) the stress state indication based on the smooth Heaviside function with $\alpha = 0.1$ and $\alpha = 0.001$.

3.2 HPI based stress constraint

A single stress constraint can be constructed based on the indicator function (9) as

$$g \equiv \int H(\frac{\sigma^{\mathrm{v}} - \bar{\sigma}}{\bar{\sigma}})\mathrm{d}\Omega = 0. \tag{11}$$

This constraint integrates the indicator function (9) over the design domain Ω. When the constraint is satisfied, it can guarantee the von Mises stress in all finite elements to be within the safe limit. However, this constraint is not differentiable. Hence, the global stress constraint is relaxed based on the smooth Heaviside function as follows

$$g_H \equiv \int H_\alpha(\frac{\sigma^{\mathrm{v}} - \bar{\sigma}}{\bar{\sigma}})\mathrm{d}\Omega \leq \epsilon. \tag{12}$$

When the smooth Heaviside function is used, even if the stress is smaller than the limit, it would still contribute a small positive value to the integral g_H. This is to say, g_H would be positive while all the local stress constraints are satisfied. That is why a small positive number ϵ is used to bound the integral g_H. The selection of the integral bound ϵ is the key to effectively enforce the stress constraint and it determines whether a conservative design can be obtained. For better selection of ϵ and penalization of high stress concentration, we develop a general stress constraint as

$$g_H \equiv \frac{\int H_\alpha(\frac{\sigma^{\mathrm{v}}-\bar{\sigma}}{\bar{\sigma}})(\frac{\sigma^{\mathrm{v}}}{\bar{\sigma}})^{\eta_h}\mathrm{d}\Omega}{\int \mathrm{d}\Omega} \leq \epsilon, \tag{13}$$

where η_h is the stress penalty factor. By normalizing the numerator with the total volume of the design domain, the selection of ϵ would be less sensitive to design problems. Then the parameters of a benchmark problem can be used as a reference for other problems. Further, defined in this way, g_H will have physical meanings. By choosing $\eta_h = 0$, the g_H approximately represents the volume fraction of the material that would yield. Similarly, we can define g_H as volume fraction of the the squared von Mises stress that exceeds the limit when $\eta_h = 2$. In the following, we will briefly discuss the physical meaning and the selection of the parameters α, ϵ and η_h in the stress constraint (13). The effects of these parameters will be explicitly illustrated by numerical examples in Section 6.1.

The Heaviside parameter α The parameter α controls the sharpness of the Heaviside function H_α. With large α, since the 0/1 transition occurs slowly, $H_\alpha(\frac{\sigma^{\mathrm{v}}-\bar{\sigma}}{\bar{\sigma}})$ cannot precisely represent the stress state of the elements. In such a case, a large number of low stresses would contribute a relatively large value to the integral g_H in (13). As a result, when the constraint (13) is applied to push the maximum stress to be lower than the limit, low stresses have to be very small. This means a excessively conservative design would be obtained. When α approaches 0, $H_\alpha(\frac{\sigma^{\mathrm{v}}-\bar{\sigma}}{\bar{\sigma}})$ can clearly identify the stresses exceeding the limit. Hence, the constraint (13) can efficiently control the local stress level. However, too small α would make the Heaviside function very steep. This would lead to high nonlinearity of the stress constraint and make the optimization algorithm unstable. On balance and through numerical experiments, a relative small value (i.e. 0.005) is suggested in our work.

The integral bound ϵ For the given η_h and α, one can find an appropriate ϵ in (13) to guarantee all the local stress constraints to be satisfied. If the ϵ is too large, the local stress constraints would be violated; if the ϵ is too small, a excessively conservative design would be obtained. Based on the fact that smaller ϵ gives more conservative design, an adaptive scheme is proposed to select an appropriate ϵ. The ϵ is initially set to ϵ^0 in the first fifty iterations and then it is updated every ten iterations as

$$\epsilon^{k+1} = \min(\frac{\bar{\sigma}}{\hat{\sigma}^{\mathrm{v}}_{\max}}\epsilon^k, \epsilon^k), \tag{14}$$

where ϵ^{k+1} and ϵ^k represent the value of ϵ in the successive steps and $\hat{\sigma}^{\mathrm{v}}_{\max}$ is the average of the maximum stresses in the previous five iterations. We select an average value of the maximum stress rather than a value at one iteration in order to avoid oscillations in the optimization convergence. This unpdate stragegy would make the stress constraint tighter during the optimization and keep pushing failed materials away from the design. Finally, as the maximum stress maintains within the prescribed limit, ϵ would keep as a constant value, and make the algorithm converged.

The penalty power η_h As we set $\eta_h > 0$, the parameter η_h is similar with the aggregation parameter P in the p-norm aggregation and then $H_\alpha(\frac{\sigma^{\mathrm{v}}-\bar{\sigma}}{\bar{\sigma}})$ can be seen as the weights. The constraint (13) now also has a flavor of the low-order p-norm. Large η_h can be used to penalize high stress concentration, but it will increase the nonlinearity of the optimization problem as well. Hence small η_h is preferred for better convergence. However, if η_h is set to zero, the stress constraint (13) will force the material to change between two states, safe or failed. This fact will make the optimization algorithm unstable and more sensitive to the selection of ϵ. Therefore, unless otherwise specified, $\eta_h = 2$ is suggested in our work for both low nonlinearity and stable convergence of the optimization problem.

3.3 Multiple load cases

In realistic situation, it may need to consider multiple load cases [18, 7, 19]. The proposed stress constraints can also be easily extended to multiple load cases. A straightforward scheme is to define a global constraint as in (13) for each load case. For a structure subject to a number N_l of load cases, we define stress constraint for each load case l, $l = 1, ..., N_l$, as

$$g^l_H \equiv \frac{\int H_\alpha(\frac{\sigma^{\mathrm{v}}_l-\bar{\sigma}_l}{\bar{\sigma}_l})(\frac{\sigma^{\mathrm{v}}_l}{\bar{\sigma}_l})^{\eta_h}\mathrm{d}\Omega}{\int \mathrm{d}\Omega} \leq \epsilon_l, \quad \text{for } l = 1, ..., N_l. \tag{15}$$

In our work, the stress limit $\bar{\sigma}_l$ is assumed to be the same for all load cases. But it is straightforward to consider different $\bar{\sigma}_l$ for different load cases. In the first scheme, we may need to define the bound ϵ_l for each load case if the design is asymmetric under different load cases.

Another scheme is to group all the stress constraints for different load cases into a single global constraint. That is, we define the global stress constraint as

$$g_H \equiv \sum_{l=1}^{N_l} \frac{\int H_\alpha(\frac{\sigma^{\mathrm{v}}_l-\bar{\sigma}_l}{\bar{\sigma}_l})(\frac{\sigma^{\mathrm{v}}_l}{\bar{\sigma}_l})^{\eta_h}\mathrm{d}\Omega}{\int \mathrm{d}\Omega} \leq \epsilon. \tag{16}$$

In the second scheme, we only need to define one bound ϵ to guarantee effectiveness of stress constraint. However, as the number of load cases increases, a single stress constraint can lose its ability to control local stresses.

In our work, both schemes are implemented and applied to the design a L-bracket with multiple load cases (see Section 6.2).

3.4 Computational cost analysis

From the view point of computational cost, the HPI based approach has an advantage over the conventional approaches based on the KS and p-norm aggregations. In the following, the average time at each iteration are estimated for the HPI based approach and the KS and p-norm aggregations. As the KS and p-norm aggregations work in a similar way, we only analyze the computational cost for the p-norm function. When doing computational cost comparison, it is assumed that based on the HPI approach, one single constraint can work as effective as multiple groups with the p-norm aggregation. The computational cost is mainly spent on solving the forward equation, the adjoint equation and the optimization system. It reads

$$T = T_{\text{fwd}}(N) + T_{\text{adj}}(n_g, N) + T_{\text{opt}}(n_g, N), \tag{17}$$

where $T_{\text{fwd}}, T_{\text{adj}}$ and T_{opt} represent the time for the forward equation, the adjoint equation and the optimizer, respectively. Both T_{adj} and T_{opt} depend on the number of groups for stress constraints, n_g, and the total number of elements, N. Since the time for solving each adjoint equation are equal, we have

$$T = T_{\text{fwd}}(N) + n_g T_{\text{adj}}(N) + T_{\text{opt}}(n_g, N). \tag{18}$$

In practice, the time for solving the forward and adjoint equations are comparable. Further, the time for solving the optimization system is negligible compared with the time for solving state equations. That is

$$T_{\text{fwd}}(N) \approx T_{\text{adj}}(N), \tag{19}$$

$$T_{\text{opt}}(n_g, N) \ll T_{\text{fwd}}(N). \tag{20}$$

The number of stress constraints for the HPI based approach and the p-norm aggregation reads

$$n_g = \begin{cases} 1 & \text{for} \quad \text{HPI} \\ \dfrac{N}{M} & \text{for} \quad \text{p-norm}, \end{cases} \tag{21}$$

where M is the number of local constraints in each aggregation group. Hence, the ratio between the time of the p-norm aggregation and the time of the HPI based approach reads

$$\frac{T^{\text{pnorm}}}{T^{\text{HPI}}} \approx \frac{1 + N/M}{2}. \tag{22}$$

As N is fixed for any specific problem, the time for the HPI based approach is also fixed and the time for the KS or p-norm aggregations depends on the number of local constraints in each aggregation group, i.e. M. In order to effectively control the local stress level efficiently, M should not be too large. In density-based topology optimization considering stress constraints, M should be close to 1000 based on our numerical experiments and observations in literatures [7, 13]. Therefore, for a large-scale problem, as N/M in (22) becomes large, the time saved by the HPI approach would be tremendous. In Section 6.1, the computational cost is further investigated through numerical experiments.

4 Optimization formulations

In our work, we minimize the volume subject to stress constraints. Based on the Heaviside projection based integral, the proposed approach only has one stress constraint (13) and the optimization formulation reads

$$\min_{\rho} \quad J = \int \bar{\rho} \mathrm{d}\Omega \tag{23a}$$

$$\text{s.t.} \quad \int_{\Omega} E(\bar{\rho}) \mathbf{s}(\mathbf{u}) \cdot \nabla \widetilde{\mathbf{u}} \mathrm{d}\Omega = \int_{\Omega} \mathbf{b} \cdot \widetilde{\mathbf{u}} \mathrm{d}\Omega + \int_{\Gamma_t} \mathbf{t} \cdot \widetilde{\mathbf{u}} \mathrm{d}\Gamma, \quad \forall \widetilde{\mathbf{u}} \in \widetilde{V} \tag{23b}$$

$$(13) \tag{23c}$$

$$0 \leq \rho \leq 1. \tag{23d}$$

In this formulation, (23a) and (23c) denote the material volume and the stress constraint, respectively. (23b) defines the weak form of the linear elasticity problem. $\mathbf{b}$ is the body force, $\mathbf{t}$ is the traction applied on boundary Γ_t. $\widetilde{\mathbf{u}}$ is the test function of the displacement, and $\widetilde{V}$ is the space of $\widetilde{\mathbf{u}}$. It reads

$$\widetilde{V} = \left\{ \widetilde{\mathbf{u}} \in [H^1(\Omega)]^3 : \widetilde{\mathbf{u}} = \mathbf{0} \text{ on } \Gamma_{\mathrm{D}} \right\},$$

where Γ_D is the Dirichlet boundary on which the displacement is prescribed.

In our work, the Solid Isotropic Material interpolation with Penalization (SIMP) method [20] is applied to solve the optimization problem (23). And the stress tensor (1) is denoted as

$$\boldsymbol{\sigma}(\mathbf{u}) = E(\bar{\rho}) \mathbf{s}(\mathbf{u}), \tag{24}$$

where $\mathbf{s}(\mathbf{u})$ is the stress tensor for unit Young's modulus. $E(\bar{\rho})$ denotes the Young's modulus for the physical density $\bar{\rho}$ and it reads

$$E(\bar{\rho}) = E_{\min} + (E_0 - E_{\min}) \bar{\rho}^q, \tag{25}$$

where E_0 is the Young's modulus for the solid material, $E_{\min}$ is a small number to avoid the singularity in finite element matrices and q is the SIMP power factor. In our implementation, $E_{\min}$ and q are set to 1e$-$9 and 3, respectively.

To avoid numerical instability and control the minimum length scale, we use the density filter based on the Helmholtz PDE [21]

$$-r^2 \nabla^2 \widetilde{\rho} + \widetilde{\rho} = \rho, \tag{26}$$

where $\widetilde{\rho}$ is the filtered density and r controls the length scale. The parameter r corresponds to the filter radius $2\sqrt{3}r$ in the classic density filtering [21].

In order to obtain clear topology without intermediate materials, the Heaviside filter proposed in [22] is also adopted in our work. Then the physical density $\bar{\rho}$ is given by

$$\bar{\rho} = \begin{cases} \xi \left[\mathrm{e}^{-\beta(1-\frac{\widetilde{\rho}}{\xi})} + (1 - \frac{\widetilde{\rho}}{\xi}) \mathrm{e}^{-\beta} \right] & 0 \leq \widetilde{\rho} \leq \xi \\ (1-\xi) \left[1 - \mathrm{e}^{-\beta \frac{\widetilde{\rho}-\xi}{1-\xi}} + (\frac{\widetilde{\rho}-\xi}{1-\xi}) \mathrm{e}^{-\beta} \right] & \xi \leq \widetilde{\rho} \leq 1, \end{cases} \tag{27}$$

where ξ is the threshold and β is the parameter to control the sharpness the Heaviside projection in (27). When a large value of β is given, the Heaviside filter (27) forces the filtered density $\widetilde{\rho}$ smaller than ξ moving towards to 0 and $\widetilde{\rho}$ larger than ξ to 1.

In order to show the validity and advantages of our approach to stress constrained problem, we compare it with the KS and p-norm aggregations. In our implementation of the KS and p-norm approaches, the active-set based strategy introduced in [14] is employed to aggregate local stresses and the adaptive normalization scheme proposed in [7] is utilized to narrow the gap between the maximum stress and the stress limit.

5 Sensitivity analysis

For the gradient-based optimization method, sensitivity analysis of the objective function and constraints is necessary. In this section, we discuss the sensitivity derivation of the Heaviside projection integral g_H in (13), based on which we construct the stress constraint. The sensitivity of g_H can be derived by using the chain rule. As the sensitivity of physical density $\bar{\rho}$ with respect to optimization variables ρ can be easily obtained by differentiating (26) and (27), we only explain in detail the sensitivity analysis of g_H with respect to physical density $\bar{\rho}$ herein.

The Lagrange functional adjointing the Heaviside projection integral g_H in (13) and the linear elasticity equation reads

$$\mathcal{L} = \frac{\int H_\alpha(\frac{\sigma^{\mathrm{v}}-\bar{\sigma}}{\bar{\sigma}})(\frac{\sigma^{\mathrm{v}}}{\bar{\sigma}})^{\eta_h}\mathrm{d}\Omega}{\int \mathrm{d}\Omega} + \int \mathbf{v}\cdot(\nabla\cdot\boldsymbol{\sigma}+\mathbf{b})\mathrm{d}\Omega, \tag{28}$$

where $\mathbf{v}\in\widetilde{V}$ is the adjoint variable for the elasticity equation. Similar with the deviation of the weak formulation (23b), we have

$$\mathcal{L} = \frac{\int H_\alpha(\frac{\sigma^{\mathrm{v}}-\bar{\sigma}}{\bar{\sigma}})(\frac{\sigma^{\mathrm{v}}}{\bar{\sigma}})^{\eta_h}\mathrm{d}\Omega}{\int \mathrm{d}\Omega} + \int_\Omega \nabla\mathbf{v}\,:\,E(\bar{\rho})\mathbf{s}(\mathbf{u})\mathrm{d}\Omega - \int_\Omega \mathbf{b}\mathbf{v}\mathrm{d}\Omega - \int_{\Gamma_t}\mathbf{t}\mathbf{v}\mathrm{d}\Gamma. \tag{29}$$

By setting the directional derivative of $\mathcal{L}$ with respect to the state variable $\mathbf{u}$, $\frac{\partial\mathcal{L}}{\partial\mathbf{u}}$, to be zero, the adjoint equation can be obtained and it reads

$$\int H'_\alpha(\frac{\sigma^{\mathrm{v}}-\bar{\sigma}}{\bar{\sigma}})\frac{\sigma^{\mathrm{v}}_{,\mathbf{u}}}{\bar{\sigma}}(\frac{\sigma^{\mathrm{v}}}{\bar{\sigma}})^{\eta_h}\mathrm{d}\Omega + \int H_\alpha(\frac{\sigma^{\mathrm{v}}-\bar{\sigma}}{\bar{\sigma}})\eta_h(\frac{\sigma^{\mathrm{v}}}{\bar{\sigma}})^{\eta_h-1}\frac{\sigma^{\mathrm{v}}_{,\mathbf{u}}}{\bar{\sigma}}\mathrm{d}\Omega + \int_\Omega \nabla\mathbf{v}\cdot E(\bar{\rho})\mathbf{s}(\widetilde{\mathbf{u}})\mathrm{d}\Omega = 0. \tag{30}$$

In (30), $\sigma^{\mathrm{v}}_{,\mathbf{u}}$ denotes the directional derivative of σ^{v} with respect to $\mathbf{u}$

$$\sigma^{\mathrm{v}}_{,\mathbf{u}} = \frac{\partial\sigma^{\mathrm{v}}}{\partial\mathbf{u}} = \frac{3}{2\sigma^{\mathrm{v}}}\boldsymbol{\sigma}^{\mathrm{d}}(\mathbf{u})\cdot\boldsymbol{\sigma}^{\mathrm{d}}(\widetilde{\mathbf{u}}),$$

and $H'_\alpha(x)$ represents the derivative of H_α

$$H'_\alpha(x) = \frac{\alpha}{\pi(x^2+\alpha^2)}. \tag{31}$$

By solving the adjoint equation (30), we can obtain the adjoint variable $\mathbf{v}$. Then the sensitivity of the Heaviside projection integral g_H reads

$$\mathcal{L}'_{,\bar{\rho}} = \int H'_\alpha(\frac{\sigma^{\mathrm{v}}-\bar{\sigma}}{\bar{\sigma}})\frac{\sigma^{\mathrm{v}}_{,\bar{\rho}}}{\bar{\sigma}}(\frac{\sigma^{\mathrm{v}}}{\bar{\sigma}})^{\eta_h}\mathrm{d}\Omega + \int H_\alpha(\frac{\sigma^{\mathrm{v}}-\bar{\sigma}}{\bar{\sigma}})\eta_h(\frac{\sigma^{\mathrm{v}}}{\bar{\sigma}})^{\eta_h-1}\frac{\sigma^{\mathrm{v}}_{,\bar{\rho}}}{\bar{\sigma}}\mathrm{d}\Omega + \int_\Omega \nabla\mathbf{v}\cdot E'_{,\bar{\rho}}(\bar{\rho})\delta\bar{\rho}\mathbf{s}(\widetilde{\mathbf{u}})\mathrm{d}\Omega, \tag{32}$$

where $\delta\bar{\rho}$ denotes the variation of $\bar{\rho}$. The derivative of σ^{v} over $\bar{\rho}$ can be obtained from (2) as

$$\sigma^{\mathrm{v}}_{,\bar{\rho}} = \eta'_{,\bar{\rho}}(\bar{\rho})\delta\bar{\rho}\sigma^{\mathrm{v}}_0.$$

In (32), $E'_{,\bar{\rho}}$ denotes the derivative of E over $\bar{\rho}$ and it reads

$$E'_{,\bar{\rho}} = q(E_0 - E_{\min})\bar{\rho}^{q-1}. \tag{33}$$

It should be noted that for each stress constraint, one adjoint equation as (30) has to be solved to calculate its sensitivities. Therefore, to derive the sensitivities of stress constraints, we solve only one adjoint equation in our approach. But for the KS and the p-norm based approaches, we need to solve n_g number of adjoint equations.

6 Numerical examples

In this section, details on numerical implementation are discussed. Numerical examples are also presented to demonstrate the effectiveness and efficiency of the proposed approach to stress-constrained topology optimization.

The work is implemented in FEniCS [23], which is an open source finite element solver and can automatically solve differential equations based on the defined weak formulations. In our implementation, linear triangular or tetrahedral elements are used to discretize the design domain. All the optimization variables ρ, the filtered density $\tilde{\rho}$ and the physical density $\bar{\rho}$ are finite element nodal based. The initial optimization variables are set to 0.5 for all the numerical examples.

The method of moving asymptotes (MMA) [24] is used as the optimizer. Since the stress constraints are highly nonlinear, a relative small move limit is selected to make the optimizer more conservative. The move limit is set to 0.1 in our implementation. The optimization algorithm terminates when the maximum change of optimization variables is less than 0.01 or else when the number of iterations exceeds 350.

For the Helmholtz filtering (26), the length-scale control parameter r is selected such that the effective filter radius corresponds to 1.5 times the element size in the classical density filtering. For the Heaviside filtering (27), ξ is set to 0.5. As β controls the steepness of the Heaviside filter, it is initialized to be 1.0 and increases by 1.0 every 25 iterations until reaching 10. As mentioned before, the stress constrained problem is highly nonlinear. Hence, we choose a relative small upper bound of β to achieve stable convergence. It turns out that this selection of β suffices to obtain black-and-white layouts.

In the following, a 2D L-shaped bracket is first studied to verify the HPI based stress constraint (13), to investigate the selection of its parameters and to show its advantages over the classical KS and p-norm aggregations. Then a 2D L-bracket subject to multiple load cases is presented. In the third example, a 2D MBB beam is investigated to further validate the proposed approach. Finally, we use the design of a 3D L-bracket to demonstrate that the proposed stress constraint is applicable to 3D problems.

6.1 2D L-bracket

The 2D L-bracket design is a popular test problem in stress constrained topology optimization. It is because that the final design of the L-shaped bracket will contain a sharp corner that can lead to high stress concentration if the stress constraints are invalid. This

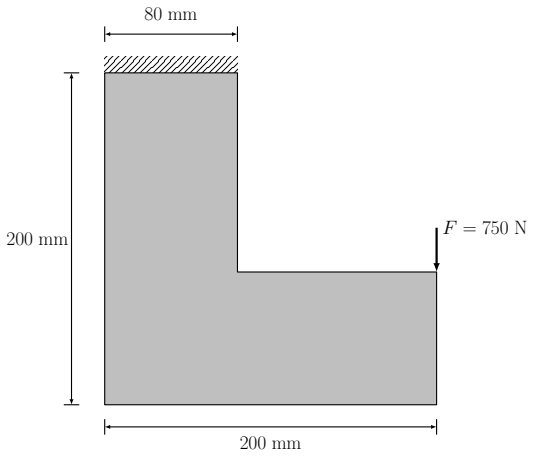

Figure 3: Design specification of the 2D L-Bracket problem.

problem is also used here to show the effectiveness and efficiency of the HPI based stress constraint. If the constraint is effective, the maximum stress in the optimized design would be smaller than the prescribed limit. Further, if the constraint is efficient in control local stress states, the optimized design would be fully-stressed. As we minimize the volume under stress constraints, this fully-stressed design would have a smaller volume.

The design model for the 2D L-bracket is shown in Fig. 3. For verification, the same dimension, loading conditions and material properties are used as in [13]. The plane stress assumption is applied for the problem and the thickness of the structure is 1 mm. The top boundary of the design domain is totally fixed. A load of magnitude 750 N is applied to the right corner of the L-shaped bracket. To avoid the stress singularity at the right corner, the load is distributed over a length of 4 mm in our implementation. The chosen material is aluminum 7075-T6, which is widely used in aircraft and aerospace structures. The Young's modulus is 68.9 GPa and the Poisson's ratio is 0.33. The yield stress is 275 MPa. The design domain is discretized with 6456 linear triangular elements. The mesh contains 3356 vertices, that is, the number of optimization variables is also 3356.

In the following, we first study the selection of parameters in the Heaviside projection integral based stress constraint (13). With all the parameters appropriately selected, a conservative and near fully-stressed design is obtained . Then we optimize the L-bracket by using the KS and p-norm aggregations and show the advantage of our approach by comparison.

6.1.1 Parameters selection

The effectiveness of the stress constraint in (13) depends on the selection of the Heaviside parameter α, the integral bound ϵ and the stress penalty factor η_h. The α controls the slope of the smoothed Heaviside function and thus exacts the level of the conservativeness of the final design. The ϵ is the most important parameter which determines whether the local stress constraints can be guaranteed or not. With different η_h, the Heaviside projection integral g_H (13) would have different physical meanings. The η_h is somewhat similar to the aggregation parameter P in the p-norm function, which reflects the domination of the high stresses. In our implementation, it turns out that $\eta_h = 2$ can already work efficiently. For a large problem, a larger η_h may be required to further penalize high

stresses. In the following, we first investigate the effects of α and ϵ on the optimization results with $\eta_h = 2$. Then the selection of η_h is explained.

The Heaviside parameter α For the given $\epsilon = 0.001$, the optimization results with $\alpha = 0.01$, $\alpha = 0.005$, and $\alpha = 0.0025$ are shown in Fig. 4. We can observe that with large α, more conservative design is obtained. That is, as α increases, the final design will use more material and have smaller stresses. The reasons can be explained as following. The larger α reduces the sharpness of the smoothed Heaviside function (10). Then the stresses smaller than the prescribed limit will contribute more to the Heaviside projection integral g_α. As a result, for the given right hand side bound ϵ, the overall stress level has to be reduced in order to satisfy the stress constraint (13). It can also be observed from Fig. 4 that with a very small α (e.g. 0.0025), the final design is near full-stressed. This is because small α increases the steepness of the Heaviside function, and then the global stress constraint can efficiently control the local stresses. However, too small α will lead to high nonlinearity of the stress constraint and thus make the optimization convergence unstable. Therefore, in our work α is set to 0.005, with which the final design is near fully-stressed and the optimization convergence is stable.

The integral bound ϵ In the following, the effects of ϵ on the final design are first investigated, then an adaptive scheme is presented to select ϵ. With $\alpha = 0.005$ and $\eta_h = 2$, Figure 5 shows the final designs for the different values of ϵ. We can observe that with a smaller ϵ, the optimized design has a smaller maximum stress and larger volume. Although non-zero ϵ allows for a certain amount of violation of stress constraint, since the Heaviside function provides high penalization to stresses that violate the given limit, a smaller ϵ would be more likely to push the violated stresses away from the design. Also, we can see from Fig. 5 that the maximum stress is very sensitive to the selection of ϵ. The final design becomes unacceptable when ϵ only changes from 0.0005 to 0.0025. We can observe form Fig. 5(b) with $\epsilon = 0.0025$ that the maximum stress is larger than the prescribed limit. Therefore, the selection of ϵ is very important to obtain a conservative and full-stressed design. In practice, it is difficult to preset an appropriate ϵ. If the ϵ is too small, the final design would be excessively conservative; if the ϵ is too large, the highest stress would exceed the prescribed limit.

The adaptive scheme to select ϵ presented in Section 3 is investigated. This kind of adaptive selection of ϵ not just can guarantee a conservative design but also can narrow the gap between the maximum stress and the prescribed limit. In our implementation, ϵ is set to 0.005 at the fist 25 iterations and to 0.0025 in the following 25 iterations. Then it is updated every 10 iterations by using (14). The selection of values 0.005 and 0.0025 is based on the results shown in Fig. 5. As the stress constraint (13) has been normalized by the volume of the design domain, this kind of selection can be extended to other numerical examples. Figure 6 shows the optimized results by adaptively choosing the parameter ϵ. We can observe that the maximum von Mises stress is smaller than the yield limit and the gap between them is quite small. The final design is comparable to that in [13]. In the Fig. 7, the convergence history of the volume fraction, the maximum von Mises stress and ϵ is plotted. It can be observed that although oscillations happen in the beginning, the optimization algorithm finally converges. The converged ϵ is 1.03×10^{-3}.

The penalty factor η_h The parameter η_h determines the physical meaning of the Heaviside projection integral g_α and controls the nonlinearity of the stress constraint (13).

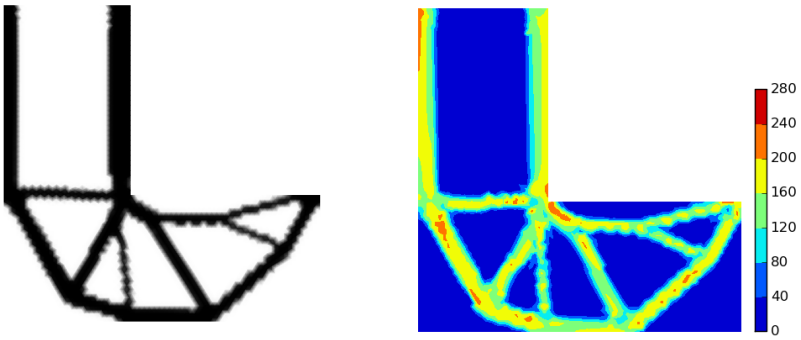

(a) $\alpha = 0.01,\ V_f = 0.303,\ \sigma^v_{\max} = 263.29$

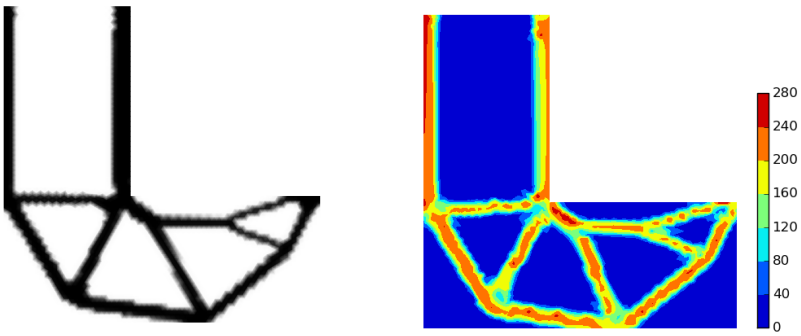

(b) $\alpha = 0.005,\ V_f = 0.257,\ \sigma^v_{\max} = 274.0$

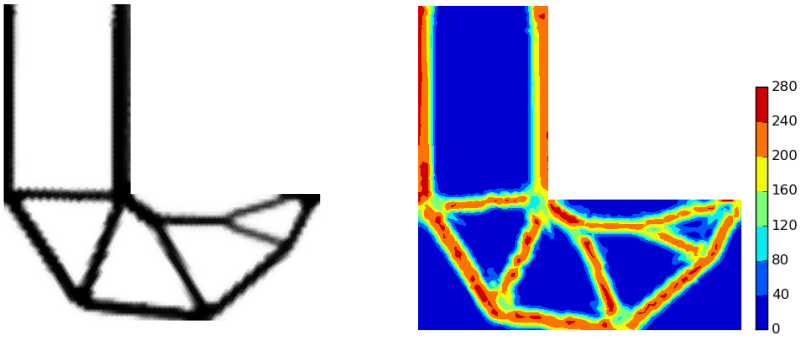

(c) $\alpha = 0.0025,\ V_f = 0.251,\ \sigma^v_{\max} = 285.07$

Figure 4: Optimized 2D L-bracket designs based on the HPI approach for different Heaviside parameters α. The integral bound ϵ is set to $\epsilon = 0.001$. On the left the density distribution, right the corresponding von Mises stress with the prescribed limit $\bar{\sigma} = 275$ MPa.

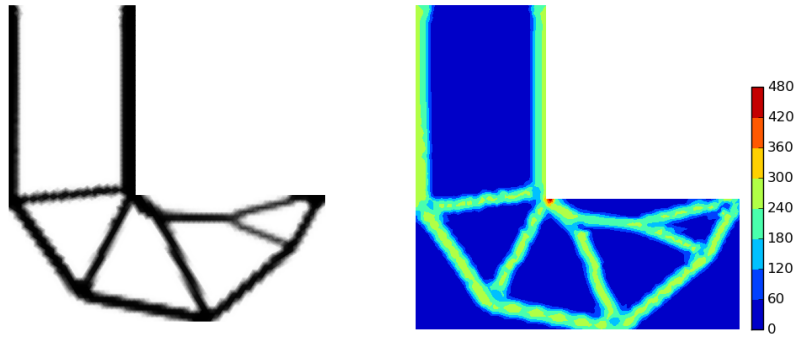

(a) $\epsilon = 0.005,\ V_f = 0.223,\ \sigma^v_{\max} = 550.86$

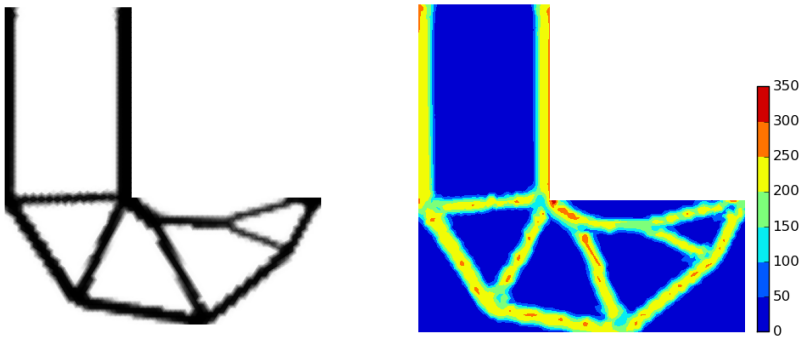

(b) $\epsilon = 0.0025,\ V_f = 0.234,\ \sigma^v_{\max} = 426.33$

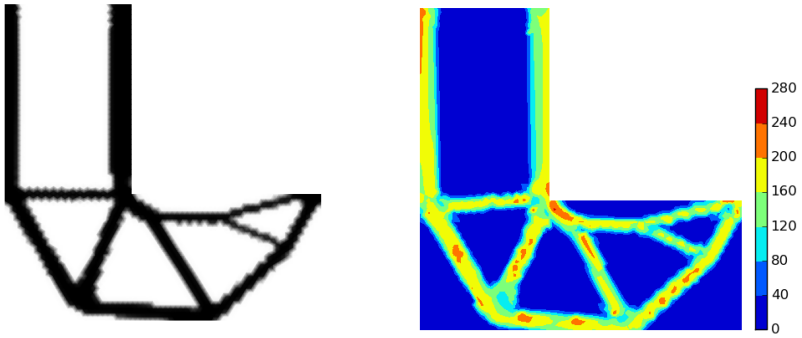

(c) $\epsilon = 0.0005,\ V_f = 0.297,\ \sigma^v_{\max} = 268.30$

Figure 5: Optimized 2D L-bracket designs based on the HPI approach for different integral bounds ϵ. The Heaviside parameter is set to $\alpha = 0.005$. On the left the density distribution, right the corresponding von Mises stress with the prescribed limit $\bar{\sigma} = 275$ MPa.

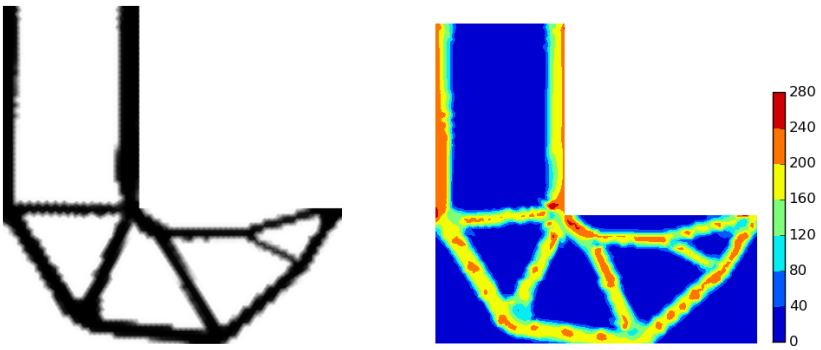

(a) $V_f = 0.276, \sigma^v_{\max} = 272.2$ (b) Von Mises stress

Figure 6: Optimized 2D L-bracket designs based on the HPI approach with the adaptively selected integral bound ϵ. (a) $V_f = 0.276$, (b) $\sigma^v_{\max} = 272.2$. The prescribed limit of the von Mises stress is $\bar{\sigma} = 275$ MPa

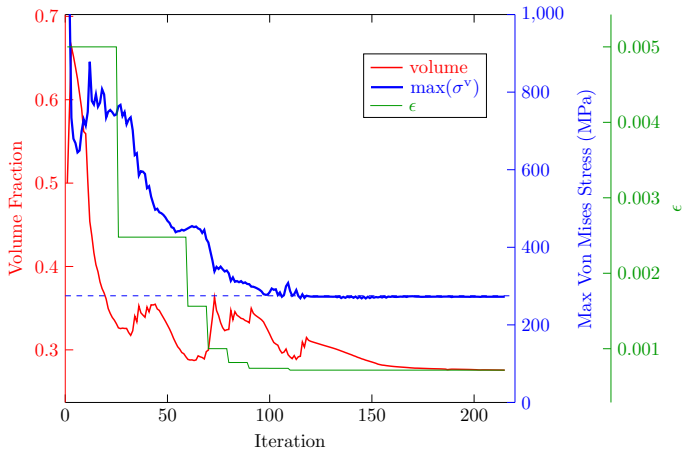

Figure 7: The convergence history for the 2D L-bracket design in Fig. 6 with the adaptively selected integral bound ϵ.

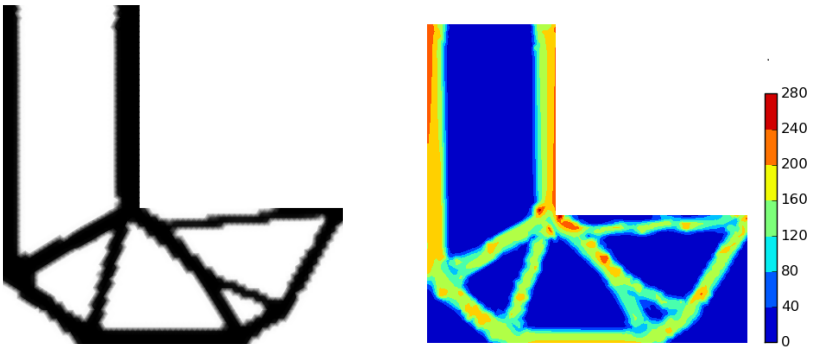

(a) $\eta_h = 0, V_f = 0.329, \sigma^v_{\max} = 263.95$

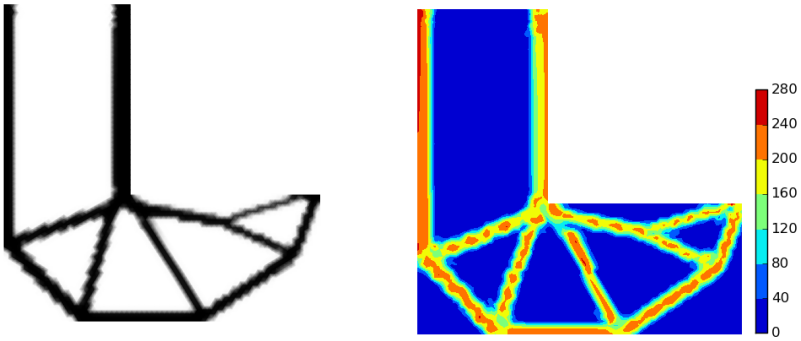

(b) $\eta_h = 4,\ V_f = 0.244,\ \sigma^v_{\max} = 273.57$

Figure 8: Optimized 2D L-bracket designs based on the HPI approach with the different penalty factors η_h. On the left the density distribution, right the corresponding elemental von Mises stress with the prescribed limit $\bar{\sigma} = 275$ MPa.

Since large η_h will cause high nonlinearity of the stress constraint (13), η_h should be as small as possible if the stress constraint can efficiently remove high stress concentration. Therefore, two more cases with $\eta_h = 0$ and $\eta_h = 4$ are investigated herein. In the study of the η_h, the α is set to 0.005 and the ϵ is adaptively selected.

Figure 8 shows the optimization results for $\eta_h = 0$ and $\eta_h = 4$. For the designs in Fig. 8, the stress constraint is satisfied. The corresponding convergence history for $\eta_h = 0$ and $\eta_h = 4$ are shown in Fig. 9. We can observe that when η_h is set to 0, a relative conservative design is obtained. This is because without the term $(\frac{\sigma^v}{\bar{\sigma}})^{\eta_h}$, the stress constraint (13) cannot control local stresses efficiently. Hence, to guarantee the maximum stress to be smaller than the prescribed limit, all other local stresses should be much smaller. Therefore, in our implementation, although η_h provides better convergence, we still set η_h to a non-zero value to further penalize high stresses. Also, a non-zero η_h can make the stress constraint (13) more stable because the stress state of one element does not have to change between two states, i.e. safe or failed. Hence, the stress constraint would be less sensitive to the selection of ϵ in (13).

When $\eta_h > 0$, the role of η_h is similar to that of the aggregation parameter P in the p-norm aggregation. With a large η_h used, the global constraint (13) can efficiently control the local stress constraints and a fully-stressed design can be obtained. This explains why the minimum volume fraction by using $\eta_h = 4$ (see Fig. 8) is smaller than that by using $\eta_h = 2$ (see Fig. 6). By comparing the convergence history shown in Fig. 9 and Fig. 7, it can also be observed that the algorithm takes more iterations to become stable and get

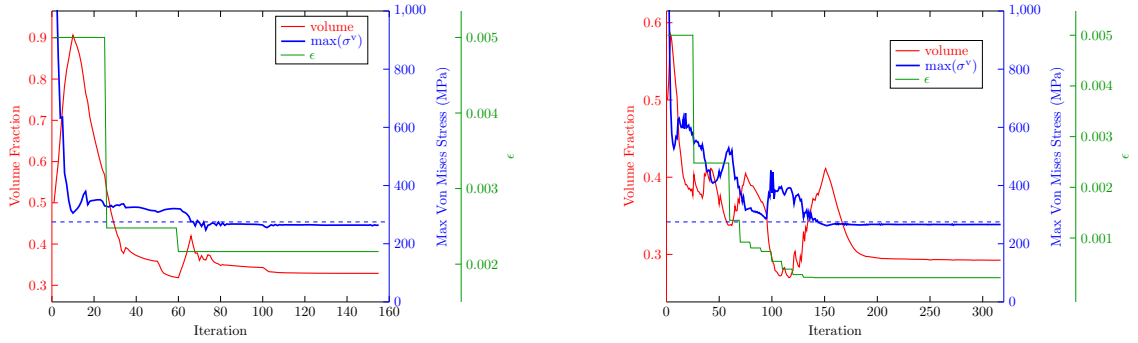

(a) $\eta_h = 0$ (b) $\eta_h = 4$

Figure 9: Convergence history of 2D L-bracket designs based on the HPI approach with the different penalty factors η_h.

converged in the case of $\eta_h = 4$. This makes sense since the large power parameter η_h can make the stress constraint (13) highly nonlinear. In addition, with the large η_h, the right hand side of the adjoint equation (30) will also become highly nonlinear and need a large number of quadrature points to assemble precisely. This means the computational cost spent on solving the adjoint equation would increase for large η_h. In summary, η_h should be as small as possible as long as it can allow the stress constraint to work efficiently. Therefore, unless otherwise specified, η_h is set to 2 in our implementation.

6.1.2 Comparison with the KS and p-norm based aggregations

In this section, the proposed approach is compared with the conventional approaches based on the KS and the p-norm aggregations. Since the KS and p-norm aggregations are the most commonly used approaches to deal with local stresses, this comparison would help to further illustrate the efficiency of the HPI approach. Based on the results in [7, 12, 13, 14] and our own numerical tests, the local stress constraints are subdivided into $n_g = 10$ aggregation groups. The aggregation parameters for the KS and the p-norm functions are set to $\eta = 10$ and $P = 8$, respectively.

The optimization results of the L-bracket based on the KS and the p-norm aggregations are shown in Fig. 10. We can observe that the maximum stress is close to the stress limit and the designs are near fully-stressed. By comparison, the design in Fig.6 has a smaller volume fraction and lower stress level. This further demonstrates the efficiency of the proposed approach in controlling the local stresses. The convergence history for the optimization algorithm based on the KS and the p-norm aggregations is plotted in Fig. 11. The convergence of the KS and the p-norm aggregations are more stable than that of the Heaviside projection integral as shown in Fig. 7. This is because the KS and the p-norm functions approximate the maximum value in each aggregation group while the Heaviside projection integral measures the summation of the violated stresses. In this sense, the stresses smaller than the maximum value in each group will have little effects on the KS and the p-norm aggregations. However, all the stresses close to the prescribed limit will affect the Heaviside projection integral.

To further investigate the difference between the HPI approach and the p-norm aggregation, we plot the Heaviside projection and the p-norm function with different parameters in Fig. 12. The parameters for the Heaviside function are same with those

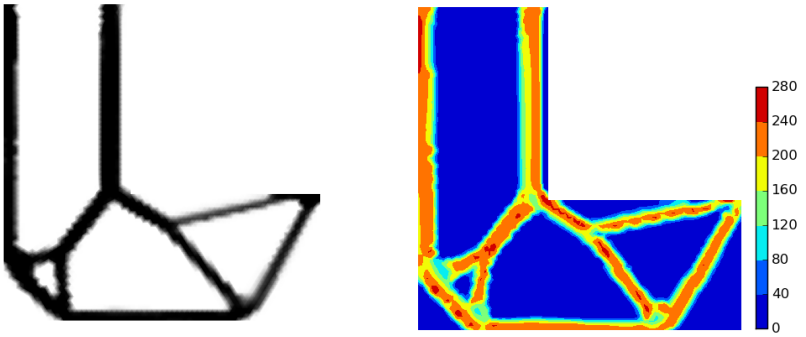

(a) KS, $V_f = 0.272$, $\sigma^v_{\max} = 275.52$

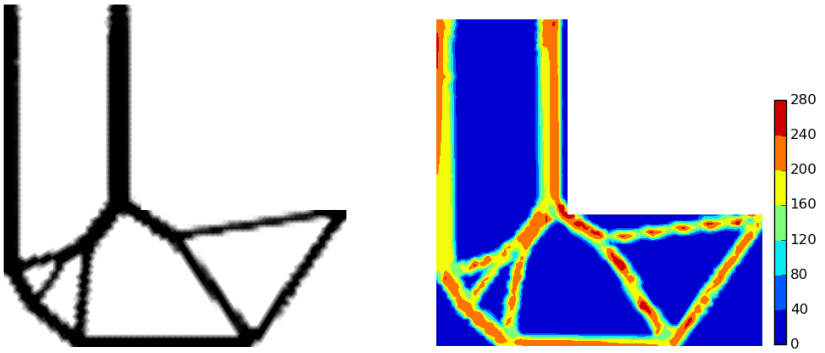

(b) p-norm, $V_f = 0.291$, $\sigma^v_{\max} = 275.36$

Figure 10: Optimized 2D L-bracket designs based on the KS and p-norm aggregations. On the left the density distribution, right the corresponding von Mises stress with the prescribed limit $\bar{\sigma} = 275$ MPa.

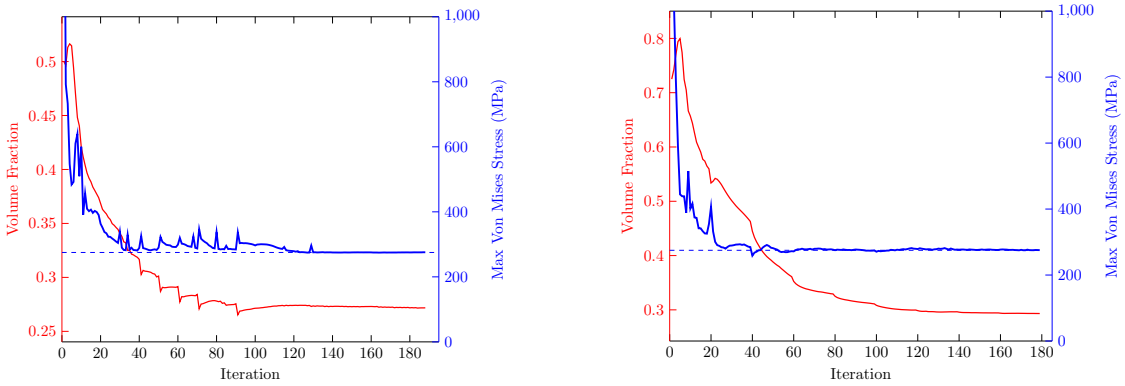

(a) KS

(b) p-norm

Figure 11: Convergence history of 2D L-bracket designs based on the KS and p-norm aggregations.

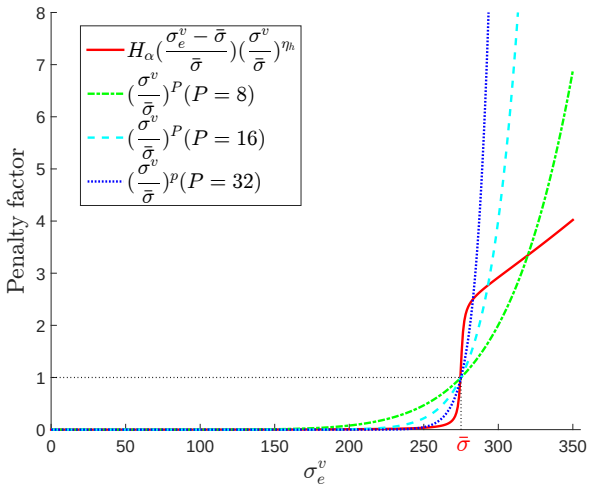

Figure 12: Penalty factor of Heaviside projection and p-norm with different parameters.

in our implementation, i.e. $\alpha = 0.005, \eta_h = 2$. It can be observed that the Heaviside function provides sharper transition close to the given limit $\bar{\sigma}$ even compared with the p-norm with large penalty parameter (e.g. $P = 32$). That is, the Heaviside function is more sensitive to the change of local stresses close to $\bar{\sigma}$. It is also should be noted that the p-norm function gives larger penalization as the stress is away from the limit. This explains that based on the p-norm aggregation, the high stresses can be quickly removed during the initial stage of the optimization (Fig. 11), but it is difficult to converge to just the limit $\bar{\sigma}$. Hence, multiple groups are frequently introduced to improve the ability of the p-norm function to identify the maximum stress in each group. Also adaptive normalization schemes, e.g. Chau et al [7], are utilized to modify stress constraint and narrow the gap between the maximum stress and the stress limit. All these strategies would increase the convergence iterations. Conversely, for the HPI approach, it is difficult to remove high stresses at the initial stage of the optimization due to relatively smaller penalization. But as the stresses become close to the limit $\bar{\sigma}$, the algorithm can also be able to identify those stresses violating the stress constraint. Thus, one single constraint can work and the convergence at the final stage of the optimization is fast. The above observations on the p-norm and the HPI approach also suggest that using the p-norm at the first stage of the optimization and the HPI approach at the latter stage could be more efficient. This would be further investigated in our future work.

As the three approaches obtain similar final designs, it makes sense to compare the computational cost. Since the KS and p-norm aggregations are similar, we use the p-norm to analyze the computational complexity in the following. First, for the given problem, we study the effects of M on the local stress level control. Figure 13 shows the optimized results with different M. We can observe from Fig. 13(a) and (b) that when M is large, the optimized design would be too conservative. Although the stress constraint is satisfied, except at the reentrant corner, the stress level is much smaller than the prescribed limit. Hence, the materials are not efficiently used and the optimized material volume would be relatively large. In comparison, when M is smaller than 1000, the local stress level can be efficiently controlled and the optimized designs become fully-stressed (see Fig. 13(c) and (d)). The optimized material volume also becomes smaller. These observations are consistent with those in [7]. Therefore, in the following, M is set to 1000 to estimate the number of groups in p-norm aggregation. It should be noted that

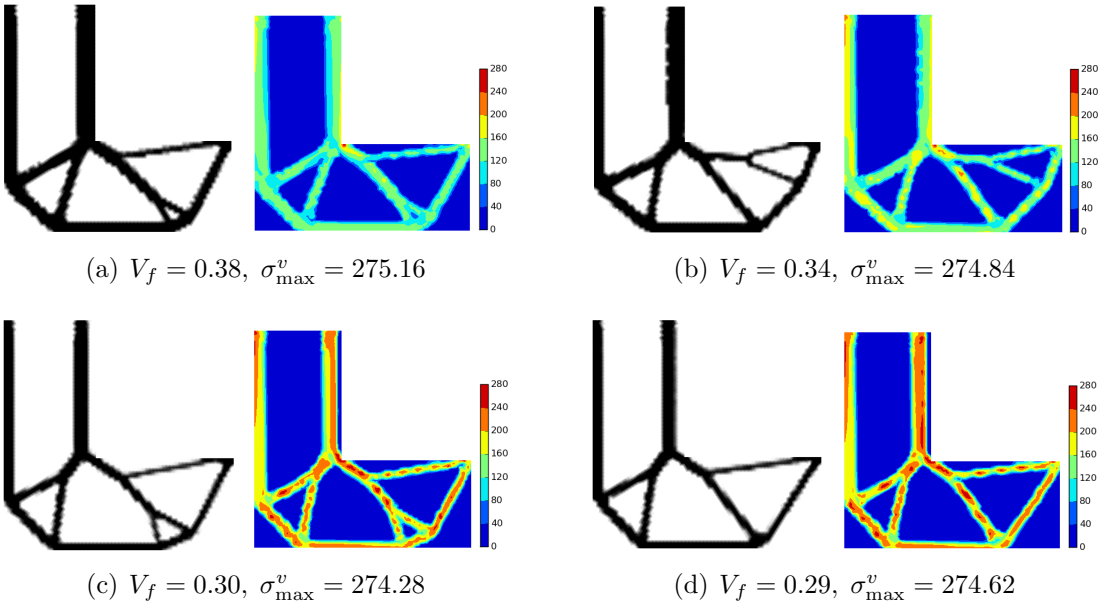

(a) $V_f = 0.38,\ \sigma^v_{\max} = 275.16$ (b) $V_f = 0.34,\ \sigma^v_{\max} = 274.84$

(c) $V_f = 0.30,\ \sigma^v_{\max} = 274.28$ (d) $V_f = 0.29,\ \sigma^v_{\max} = 274.62$

Figure 13: Optimized 2D L-bracket designs based on the p-norm aggregations with different M. The number of elements is 6446. (a) $M = 3200, n_g = 2$, (b) $M = 1600, n_g = 4$, (c) $M = 800, n_g = 8$, (d) $M = 400, n_g = 16$.

the optimized topology depends on the number of stress constraints.

We use four extra meshes to investigate the mesh independence and the computational advantage of the HPI based approach. Figure 14 shows the optimized results based on the HPI approach for the four meshes with the number of elements $11,913$, $25,824$, $47,652$ and $103,296$. We can observe that the stress constraint is satisfied for the four designs. Also, as the number of elements increases, the HPI based global stress constraint can still control the local stress level efficiently. This can be observed from the stress contours in Fig. 14 (c) and (d). Actually, the stress level of the designs in Fig. 14 (c) and (d) are close to the prescribed limit and thus smaller material volumes are achieved. Another observation is that the optimized designs for the first three meshes in Fig. 14 (a), (b) and (c) are topologically close to the design in Fig. 6. This illustrates that the HPI based approach leads to very similar designs under different mesh size.

To compare the computational cost, the p-norm aggregation is used to optimize the L-shaped bracket based on the same four sets of meshes. The number of aggregation groups, n_g, is estimated by setting $M = 1000$ in (21). If the local stress constraints cannot be efficiently controlled, n_g is further increased. The optimized designs are shown in Fig. 15. It can be observed that the stress constraint is satisfied and all the four designs are near fully-stressed. We should note that the results are highly dependent on the mesh size as we need different number of stress constraints for different meshes.

Table 1 lists the average time at each iteration, the convergence iterations N_c and the total computational time for the HPI based approach and the p-norm aggregation. Five sets of meshes are used. The corresponding optimized designs based on the HPI approach are shown in Fig. 6 and Fig. 14 and the designs based on the p-norm aggregation are shown in Fig. 10(b) and Fig. 15. As both methods can get near fully-stressed designs, it can be observed that the p-norm needs more time at each iteration. Hence, we can conclude that, for a specific problem, to achieve the same level of controlling local stresses, the HPI approach would be computationally cheap. We can also see from Table 1 that

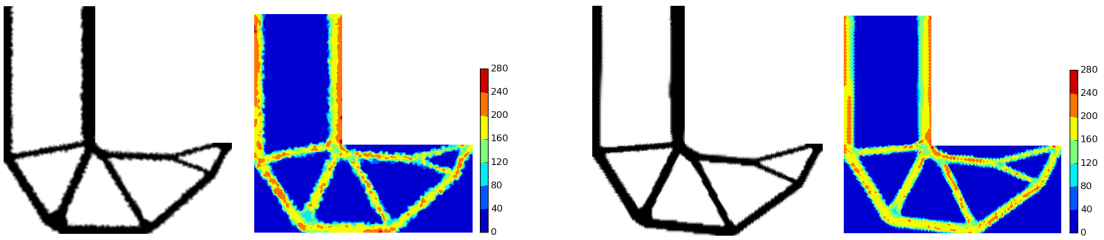

(a) $V_f = 0.268,\ \sigma^v_{\max} = 272.38$ (b) $V_f = 0.261,\ \sigma^v_{\max} = 272.73$

(c) $V_f = 0.248,\ \sigma^v_{\max} = 274.02$ (d) $V_f = 0.24,\ \sigma^v_{\max} = 272.46$

Figure 14: Optimized 2D L-bracket designs based on the HPI approach for different meshes. (a) $N = 11,913$, (b)$N = 25,824$, (c)$N = 47,652$, (d) $N = 103,296$.

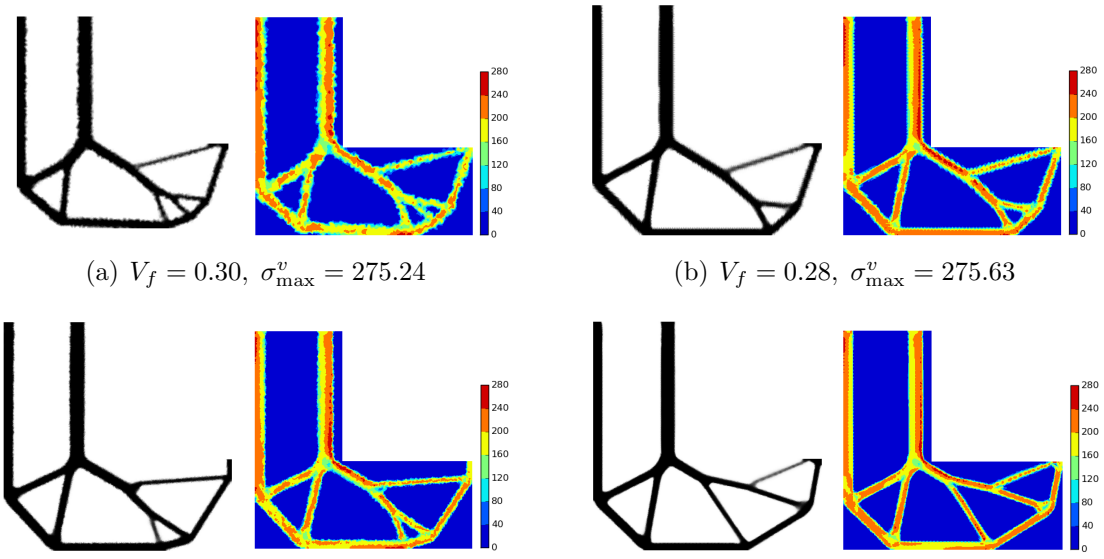

(a) $V_f = 0.30,\ \sigma^v_{\max} = 275.24$ (b) $V_f = 0.28,\ \sigma^v_{\max} = 275.63$

(c) $V_f = 0.288,\ \sigma^v_{\max} = 273.92$ (d) $V_f = 0.277,\ \sigma^v_{\max} = 274.98$

Figure 15: Optimized 2D L-bracket designs based on the p-norm aggregations for different meshes. (a) $N = 11,913, n_g = 15$, (b)$N = 25,824, n_g = 30$, (c)$N = 47,652, n_g = 50$, (d) $N = 103,296, n_g = 100$.

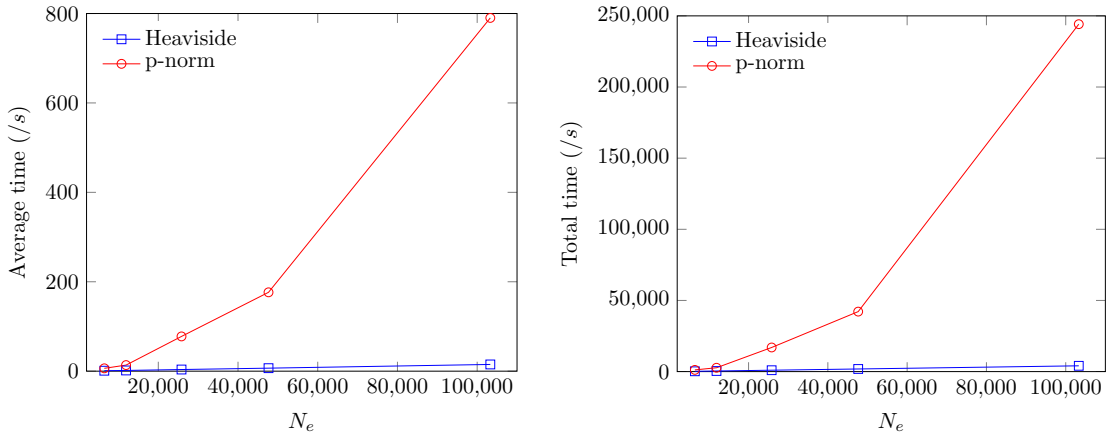

Figure 16: Computational cost(/s) of p-norm and HPI for different meshes. (a) Average time at each iteration, (b) total time.

(22) gives a good estimation of the average time ratio between the HPI approach and the p-norm aggregation. It can be also observed from Table 1 that for the p-norm aggregation, it takes more iterations to converge as the number of stress constraints increases. Hence, for large problems, the p-norm aggregation would take more iterations to converge as more stress groups are required. This means the advantage of the HPI based approach over the p-norm aggregation would be more obvious for large problems. For the fifth mesh with 103,296 finite elements, the p-norm aggregation requires up to fifty times the time for the HPI approach. Figure 16 plots both the total time and the average time over the number of elements for the five meshes. We can observe that as the time for the HPI approach increases linearly with the number of elements, the time for the p-norm aggregation increases superlinearly or quadratically.

Table 1: Computational cost(/s) of p-norm and HPI for different meshes

Elements		6,456	11,931	25,824	47,652	103,296
HPI	n_g	1	1	1	1	1
	T^{HPI}	1.02	1.63	3.66	6.70	15.04
	N_c	215	259	266	274	270
p-norm	n_g	10	15	30	50	100
	T^{pnorm}	6.35	13.01	77.73	176.37	790.19
	N_c	178	207	218	239	309
Avg. time ratio	$\frac{T^{\text{pnorm}}}{T^{\text{HPI}}}$	6.23	7.98	21.24	26.32	52.54
	$\frac{T^{\text{pnorm}}}{T^{\text{HPI}}}$ by (22)	5.5	8	15.5	25.5	50.5
Total time ratio	$\frac{T^{\text{pnorm}}.N_c}{T^{\text{HPI}}.N_c}$	5.44	6.38	17.41	22.96	60.128

It should be noted that, for the above computational cost comparison, we assume that based on the HPI approach, one single constraint can work as effective as multiple groups with the p-norm aggregation. Actually, the HPI approach could also be adapted

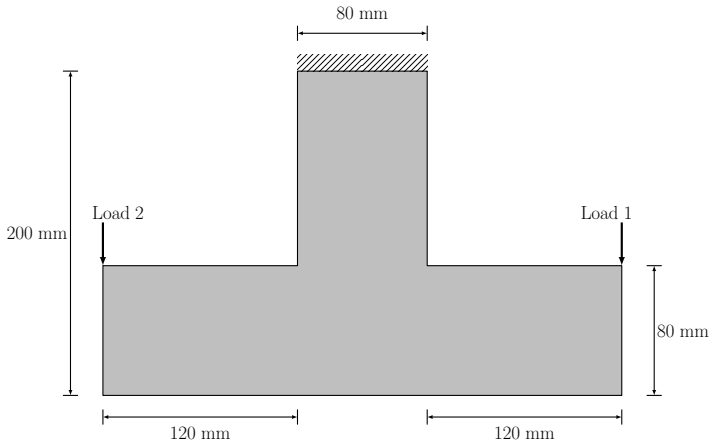

Figure 17: Design specification of a 2D L-bracket subject to multiple load cases.

with multi-groups version. If we use the same number of groups in the p-norm and the HPI, then the time spent at each iteration would be quite close. The only difference lies in how much time spent on assembling the right hand side of adjoint equations. As both the HPI and p-norm are high nonlinear, the difference of the assembling time is very small.

6.2 2D L-bracket subject to multiple load cases

In the example, a 2D L-bracket subject to multiple load cases is studied. The design specification is defined in Fig. 17. The material properties and the stress limit are same with those in the previous example. Two load cases are considered. In both load cases, the magnitude of load is same, and it is $F = 750$ N. The design domain is discretized with 16,562 linear triangular elements. The number of optimization variables is 8,501. Stress constraints are applied in two ways. In the first way, a stress constraint is constructed for each load case by (15). In the second way, a single global constraint is applied for two load cases by (16).

The optimized designs and the associated stress under two load cases are shown in Fig. 18. It can be observed that both schemes, applying stress constraint separately or together, can work efficiently. There are no high stress concentrations, and the maximum stresses are smaller than the given limit.

6.3 MBB beam

The MBB beam is another popular problem in stress-constrained topology optimization. Due to symmetry, only right half of the model is studied. Figure 19 shows the dimension and boundary conditions. The material properties and the load magnitude are same with those in [12] for verification. The material is a typical aircraft aluminum. The Young's modulus is 71,000 MPa, the Poisson's ratio is 0.33 and the yield limit is 350 MPa. The load has a magnitude of 1,500 N and is distributed over a length of 5 mm on the top left corner. The design domain is discretized with 5,022 triangular elements. The number of optimization variables is 2,613. Only the Heaviside projection integral based stress constraint is considered in the example and the selection of the parameters is same with that in the 2D L-bracket example. The Heaviside parameter α is set to 0.005, the stress

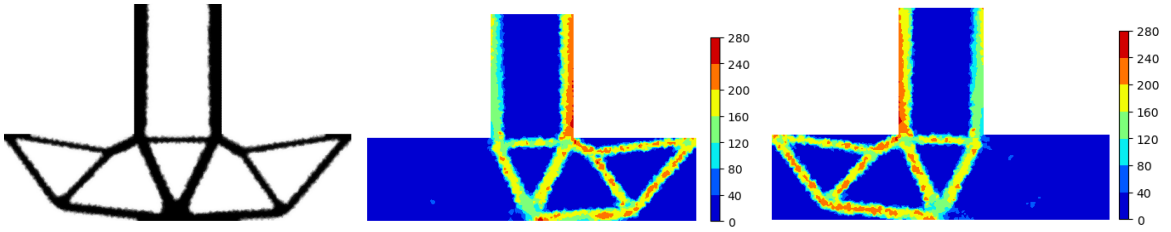

(a) $V_f = 0.28,\ \sigma^v_{1,\max} = 271.86, \sigma^v_{2,\max} = 271.40$

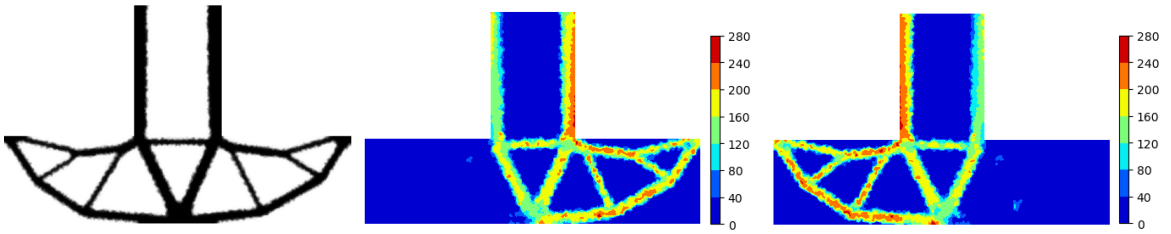

(b) $V_f = 0.29,\ \sigma^v_{1,\max} = 271.24, \sigma^v_{2,\max} = 271.99$

Figure 18: Optimized designs of the 2D L-bracket subject to multiple load cases based on the HPI approach. $\sigma^v_{l,\max}$ refers to the maximum stress for load case l. (a) Stress constraint is applied separately for each load case, (b) one single constraint is applied for two load cases.

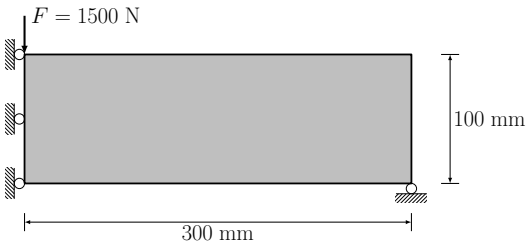

Figure 19: Design specification of the MBB beam.

penalty factor η_h is set to 2 and the integral bound ϵ is adaptively selected.

The optimized topology and the corresponding stress distribution are shown in Fig. 20. We can observe that the final design from HPI is fully-stressed and the maximum stress is smaller than the prescribed limit. This verifies the effectiveness of the proposed stress constraint. The optimized design is similar to that in [12], and the volume fraction is also comparable.

6.4 3D L-bracket

In order to demonstrate that the proposed approach is applicable to large-scale problems, a 3D L-bracket is studied. The design model of the 3D L-bracket is shown in Fig. 21. The top surface of the model is totally fixed. A pressure with a magnitude of 200 N/mm^2 is applied on the right corner. The loading surface has dimensions 40 mm by 6 mm. The material properties and the yield limit are same with those in the 2D L-bracket example. The design domain is discretized by 124,609 tetrahedron elements. The number of optimization variables is equal to the number of vertices and it is 24,367. Only one stress constraint based on the Heaviside projection integral is applied. As the number of

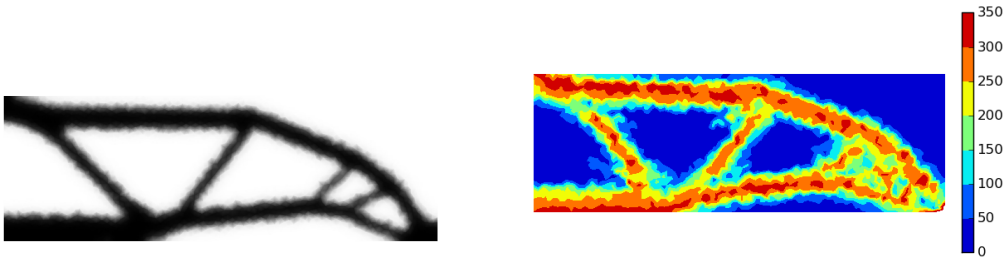

(a) Density (b) Von Mises stress

Figure 20: Optimized design of the MBB beam. (a) $V_f = 0.354$, (b) $\sigma^v_{\max} = 344.82$. The prescribed limit of the von Mises stress is $\bar{\sigma} = 350$ MPa.

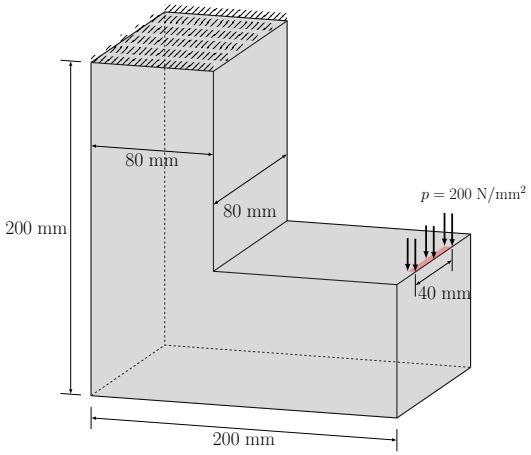

Figure 21: Design specification of the 3D L-bracket.

local stresses is large, we apply a relatively larger penalty factor, i.e. $\eta_h = 4$, to make the stress constraint (13) more sensitive to high stresses. The integral bound ϵ is set to 5×10^{-4} in the first 50 iterations, and is then adaptively updated every 10 iterations based on (14). The selection of other parameters for the stress constraint (13) is same with that in the previous examples.

The optimization results of the 3D L-bracket are shown in Fig. 22. The re-entrant corner is successfully removed from the final design. We can also observe that there is no stress concentration and the maximum stress is smaller than the given limit. This means the stress constraint works well. From the stress distribution, it can also be observed that the final design isn't as fully-stressed as that in 2D examples. This makes sense because as the number of the local stresses in the Heaviside projection integral (13) increases, its ability to control the local stress level decays to some extent.

When a single global stress constraint is used, we just need to solve one adjoint equation to derive the sensitivities. The computational time is 10.4 seconds for solving the forward equation and 8.4 seconds for the adjoint equation. If the KS and the p-norm aggregation are applied, then we need to solve about 120 adjoint equations, i.e. 120 aggregation groups are assumed, and solving each adjoint equation takes about 10 seconds. Hence, the total computational cost using the KS and p-norm aggregations would be huge and approximately 60 times of that using the Heaviside projection integral. Therefore, for this kind of 3D problems, it is much more efficient with our approach than the usual KS and the p-norm aggregations. With these usual approaches, a large number

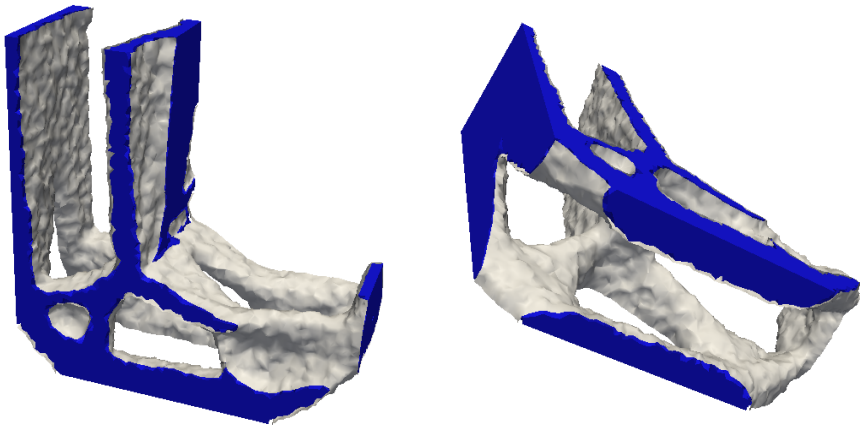

(a) Density

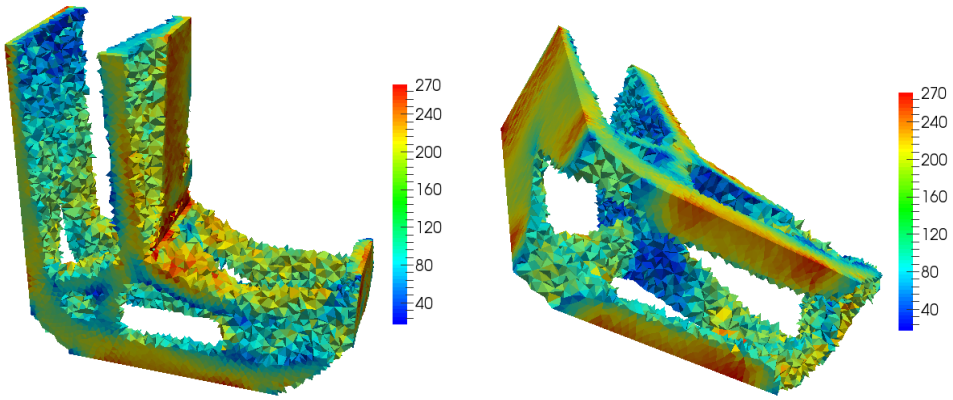

(b) Von Mises stress

Figure 22: Optimized design of the 3D L-bracket. (a) $V_f = 0.29$, (b) $\sigma^v_{\max} = 270.29$. The prescribed limit of the von Mises stress is $\bar{\sigma} = 275$ MPa.

of aggregation groups (e.g. hundreds) would be necessary in order to efficiently control the local stresses, plus each group needs to solve an adjoint problem of the same scale as the forward problem, hence the computational cost of the sensitivity analysis would be hugely prohibitive.

7 Conclusion

In the paper, an approach to stress-constrained topology optimization is proposed. A single global stress constraint is developed by using the Heaviside projection based integral of the local stresses. Such Heaviside based aggregation effectively represents the volume fraction of the material that violates the stress constraint. By constraining the integral to be smaller than a threshold value ϵ, the material region violating the stress constraint can be successfully removed from the final design. Hence, stress at every material point within the design domain will satisfy the stress constraint. The effects of the slope of the Heaviside function, the penalty factor for the local stresses and the threshold value ϵ are also studied. On the basis of our investigation, appropriate parameters for the Heaviside aggregation based stress constraint are suggested. An adaptive strategy to select ϵ is also proposed to achieve a conservative design. Both 2D and 3D numerical examples are presented to validate the proposed approach.

Compared to the traditional approaches based on the KS and the p-norm aggregations, a single global, Heaviside based stress constraint can control the local stress level efficiently in our approach. The computational cost for the sensitivity analysis is dramatically reduced as we just need to solve one adjoint equation. This advantage makes the proposed approach applicable to large scale stress problems.

8 Acknowledgment

The authors would like to thank the anonymous reviewers for their valuable comments and suggestions to improve the quality of the paper, especially for their suggestions on improving the update strategy in (14).

This work is supported in part by NSF grants 1561917 and 1404665.

References

[1] M P Bendsϕe and O Sigmund. *Topology Optimization — Theory, Methods and Applications*. Springer Verlag, Berlin, 2 edition, 2003.

[2] G Sved and Z Ginos. Structural optimization under multiple loading. *International Journal of Mechanical Sciences*, 10(10):803–805, 1968.

[3] Uri Kirsch. Optimal topologies of truss structures. *Computer Methods in Applied Mechanics and Engineering*, 72(1):15–28, 1989.

[4] Gengdong Cheng and Zheng Jiang. Study on topology optimization with stress constraints. *Engineering Optimization*, 20(2):129–148, 1992.

[5] GD Cheng and Xiao Guo. ε-relaxed approach in structural topology optimization. *Structural Optimization*, 13(4):258–266, 1997.

[6] Matteo Bruggi. On an alternative approach to stress constraints relaxation in topology optimization. *Structural and Multidisciplinary Optimization*, 36(2):125–141, 2008.

[7] Chau Le, Julian Norato, Tyler Bruns, Christopher Ha, and Daniel Tortorelli. Stress-based topology optimization for continua. *Structural and Multidisciplinary Optimization*, 41(4):605–620, 2010.

[8] Yangjun Luo, Jian Xing, Yanzhuang Niu, Ming Li, and Zhan Kang. Wrinkle-free design of thin membrane structures using stress-based topology optimization. *Journal of the Mechanics and Physics of Solids*, 2017.

[9] Panagiotis Michaleris, Daniel A Tortorelli, and Creto A Vidal. Tangent operators and design sensitivity formulations for transient non-linear coupled problems with applications to elastoplasticity. *International Journal for Numerical Methods in Engineering*, 37(14):2471–2499, 1994.

[10] Pierre Duysinx and Martin P Bendsøe. Topology optimization of continuum structures with local stress constraints. *International Journal for Numerical Methods in Engineering*, 43(8):1453–1478, 1998.

[11] RJ Yang and CJ Chen. Stress-based topology optimization. *Structural Optimization*, 12(2-3):98–105, 1996.

[12] Erik Holmberg, Bo Torstenfelt, and Anders Klarbring. Stress constrained topology optimization. *Structural and Multidisciplinary Optimization*, 48(1):33–47, 2013.

[13] Joshua D Deaton and Ramana V Grandhi. Stress-based design of thermal structures via topology optimization. *Structural and Multidisciplinary Optimization*, 53(2):253–270, 2016.

[14] Shouyu Cai and Weihong Zhang. Stress constrained topology optimization with free-form design domains. *Computer Methods in Applied Mechanics and Engineering*, 289:267–290, 2015.

[15] Kangwon Lee, Kisoo Ahn, and Jeonghoon Yoo. A novel p-norm correction method for lightweight topology optimization under maximum stress constraints. *Computers & Structures*, 171:18–30, 2016.

[16] Andrew B Lambe, Graeme J Kennedy, and Joaquim RRA Martins. An evaluation of constraint aggregation strategies for wing box mass minimization. *Structural and Multidisciplinary Optimization*, pages 1–21, 2016.

[17] Xiaoping Qian. Undercut and overhang angle control in topology optimization: a density gradient based integral approach. *International Journal for Numerical Methods in Engineering*, 2016.

[18] WM Payten and M Law. Generalized shape optimization using stress constraints under multiple load cases. *Structural optimization*, 15(3-4):269–274, 1998.

[19] Renatha B Santos, Cinthia G Lopes, and Antonio A Novotny. Structural weight minimization under stress constraints and multiple loading. *Mechanics Research Communications*, 81:44–50, 2017.

[20] M. P. Bendsøe. Optimal shape design as a material distribution problem. *Structural Optimization*, 1(4):192–202, 1989.

[21] Boyan Stefanov Lazarov and Ole Sigmund. Filters in topology optimization based on helmholtz-type differential equations. *International Journal for Numerical Methods in Engineering*, 86(6):765–781, 2011.

[22] Shengli Xu, Yuanwu Cai, and Gengdong Cheng. Volume preserving nonlinear density filter based on heaviside functions. *Structural and Multidisciplinary Optimization*, 41(4):495–505, 2010.

[23] Anders Logg, Kent-Andre Mardal, and Garth Wells. *Automated solution of differential equations by the finite element method: The FEniCS book*, volume 84. Springer Science & Business Media, 2012.

[24] K Svanberg. The method of moving asymptotes — a new method for structural optimization. *Int J Numer Methods Eng*, 24(2):359–373, 1987.